Size-Dependent Activity of Gold Nanoparticles for Oxygen Electroreduction in Alkaline Electrolyte

ARTICLE *in* THE JOURNAL OF PHYSICAL CHEMISTRY C · JUNE 2008

Impact Factor: 4.77 · DOI: 10.1021/jp710929n

Size-Dependent Activity of Gold Nanoparticles for Oxygen Electroreduction in Alkaline Electrolyte

Wei Tang,[†,||] Hongfei Lin,[‡,||] Alan Kleiman-Shwarsctein,[‡,§] Galen D. Stucky,[†,§,||] and Eric W. McFarland*[,‡,||]

Chemistry and Biochemistry Department, Department of Chemical Engineering, Materials Department, and Mitsubishi Chemical Center for Advanced Materials, University of California, Santa Barbara, California 93106

Received: November 15, 2007; Revised Manuscript Received: March 26, 2008

The dependence of the kinetics of electrocatalytic oxygen reduction in basic electrolyte on the size of Au nanoparticles was determined for 3 and 7 nm clusters supported on carbon. The size-selected nanoparticles were prepared by reverse micelle encapsulation using PS−P2VP diblock copolymer, and the kinetic current for oxygen reduction was measured with a rotating disk electrode (RDE). The kinetic current was found to be 2.5 times higher for the 3 nm gold nanoparticles compared to the 7 nm gold nanoparticles at 23 °C. The 3 nm particles were found to facilitate four-electron electroreduction, whereas a two-electron electroreduction was inferred from the RDE data on the 7 nm particles. From experiments of the temperature-dependent current the apparent activation energy for the 3 nm clusters was found to be half that of the 7 nm clusters (0.1 and 0.2 eV, respectively).

1. Introduction

Reactions of molecular oxygen on electrocatalysts have widespread applications for interconversion of chemical fuels. Most fuel cell designs utilize oxygen electroreduction on the cathode to balance the electrooxidation of fuel molecules on the anode, and electrolytic hydrogen production typically relies on anodic oxygen production. Unfortunately, the formation and decomposition kinetics of oxygen on most electrodes are relatively slow, resulting in high oxygen overpotentials required for electrolysis and fuel cell power densities significantly limited by the oxygen reduction reaction (ORR).

At present, platinum-based electrocatalysts are the most widely used material for fuel cell cathodes due to their superior performance. Pt is considered an ideal electrocatalyst due to the unique mixture of metal−adsorbate electronic interactions with oxygen bonding and antibonding orbitals which creates a unique balance of bound molecular and atomic oxygen species. Previous attempts to minimize the Pt content of electrodes for oxygen reductions led to the discovery of a significant dependence of catalytic activity on Pt particle size.[1–5] The work of Antoine et al.[1] showed the size effect for oxygen reduction in acidic medium on platinum nanoparticles, with sizes from 2.5 to 28 nm, which improves the oxygen reduction and hydrogen oxidation kinetics. Genies et al.[2] reported a 3-fold reduction in activity in alkaline electrolyte when platinum particles decreased in size from 24 to 2 nm; the increase in activity was attributed to excess HO_2^- on the surface, which is desorbed without further reduction. Mayrhofer[3] observed similar effects on platinum nanopartciles of alkaline media; however, their explanation was based on an increase in oxophilicity associated with smaller particles with OH^- blocking the active sites.

There have been several other theories for the increase in the rate of the ORR with decreased size including the model proposed by Takasu et al.[4] and Perez,[5] who explained the differences based on different ratios of Pt(100), Pt(110), and Pt(111) crystal planes present in the different size nanoparticles. The following sequence of activities for Pt single crystal surfaces were given for the ORR: Pt(110) > Pt(100) > Pt(111).

Although platinum-based catalysts have unique activity and performance for oxygen reduction, platinum will ultimately not be practical for large-scale commercialization of fuel cells or other high-volume electrodes due to the high cost and the limited supply. As one of the alternative electrocatalysts, gold was found to be reasonably active for ORR on the (100) facet on bulk gold in alkaline solutions.[6] Given the significant size effects observed for gold nanoparticles in gas phase reactions,[7] work has been done exploring the size effects of gold nanoparticles for the ORR. Guerin et al.[8] demonstrated the catalytic activity of gold on titania support in acid environment for oxygen reduction. They found that the activity reaches a maximum for a particle size of 2.5−3.0 nm. The size dependence was attributed to the strong electronic interactions between the gold particles and the oxide substrate. No previous work has been done investigating size dependence on conducting substrates suitable for fuel cells or in alkaline media where the oxygen reduction kinetics might be considerably faster than in acidic media. Further, previous synthetic methods for Au nanocluster electrocatalysts have resulted in rather broad size distributions; careful size control is necessary to better understand the details of the relationships between activity and size.

In this work the size dependence of Au electrocatalysts for the ORR in alkaline media is investigated on conducting substrates. Micelle encapsulation with diblock copolymers is used to provide a narrow size distribution.[9–11] We have addressed the following questions in this work: Are carbon-supported Au nanoclusters synthesized by micelle encapsulation active for ORR in basic media? Is there a dependence of the oxygen reduction activity in basic electrolytes on the size of the gold nanoclusters supported on carbon?

* Corresponding author. Telephone: (805) 893-4343. Fax: (805) 893-4731. E-mail: mcfar@engineering.ucsb.edu.
[†] Chemistry and Biochemistry Department.
[‡] Department of Chemical Engineering.
[§] Materials Department.
[||] Mitsubishi Chemical Center for Advanced Materials.

10.1021/jp710929n CCC: $40.75
Published on Web 06/21/2008

2. Experimental Methods

2.1. Catalyst Synthesis. The polymer solution was prepared in an N_2 purged glovebox from 25 mg of the diblock copolymer [polystyrene-*block*-poly(2-vinylpyridine)] (Polymer Source) solvated in 5 mL of toluene (Sigma Aldrich). Au nanoparticles were synthesized using polymers with two different chain lengths to achieve different size micelles: PS(54300)−P2VP(8800) and PS(53000)−P2VP(43800). The polymer solution forms micelles in which the polar poly(2-vinylpyridine) (P2VP) heads constitute the center of the micelle and the nonpolar polystyrene (PS) tails extend outward. After the solution was vigorously stirred for approximately 5 h and 8.2 mg of $HAuCl_4 \cdot 3H_2O$ was added to the solution in a dry box, the samples were prepared by drop-casting the solution of micelles onto custom-cut carbon disk electrodes (Grade 1, Ted Pella, Inc.) with a surface area of 0.2 cm^2. The polymer was removed by thermal treatment in air at 300 °C for 6 h.[9–11] To increase the surface coverage of nanoparticles, the process of drop-casting and calcination was repeated three times. High-resolution scanning electron microscopy (SEM) imaging after each calcination step showed no qualitative evidence of size changes from successive calcinations.

2.2. Electron Microscopy. The sizes of gold nanoparticles before and after calcination were characterized using a transmission electron microscope (FEI Tecnai, G2 T20 FEG Microscope). In preparing the samples for TEM, the polymer was decomposed by ozone treatment for 15 min to avoid damaging the TEM grid by the calcination used for the electrochemically characterized samples. The ozone was generated by a double bore UV lamp (Jelight Company, 0.9 W).

2.3. Determination of Au Surface Area. The active surface areas were determined by Cu-UPD (copper underpotential deposition), using the formation of a monolayer of copper on the surface of Au by the strong interaction between copper and Au.[12] These surface area values are necessary to determine the normalized current density per unit area of active electrocatalyst in the cyclic voltammograms (CVs).

2.4. Electrochemical Characterization. The RDE measurements were performed using a Pine Model MSRX RDE (Pine Research Instrumentation) equipped with a Teflon collet to hold the working electrode. Cyclic voltammograms (CVs) and linear sweep scans of potential were acquired using an EG&G 273A potentiostat (Princeton Applied Research) controlled by custom software written in LabVIEW (National Instruments). The counter electrode used in RDE experiments was a platinum wire (Alfa Aesar). The reference electrode was Ag/AgCl (in 4 M KCl) reference electrode (0.197 V vs SHE). The electrolyte for electrochemical characterization was 0.5 M potassium hydroxide (Fisher Scientific, ACS) in deionized water purged with O_2 (99.998%, Praxair) for at least 30 min prior to each measurement. The RDE measurements were conducted at a sweep rate of 10 mV s^{-1}.

To study the activity of catalysts for the ORR, the kinetic current density on the electrode was measured. To determine the kinetic current density, oxygen transport to the electrode is increased by rotating the electrode at increasingly higher rotational speeds. In general, diffusion-limited current densities for a RDE are described by the Koutecky−Levich equation:

$$\frac{1}{i} = \frac{1}{i_k} + \frac{1}{i_d}$$

where i is the total (measured) current density, i_k is the kinetic component, and i_d is the diffusion component. The diffusion component is defined as $i_d = 0.62nFD^{2/3}\upsilon^{-1/6}c_0\omega^{1/2}$, where n is the number of electrons transferred, D is the diffusion coefficient, υ is the solution viscosity, c_0 is the initial concentration, and ω is the rotation speed in radians per second.[13] The diffusion component can be simplified and expressed by the Levich equation, $i_d = Bc_0\omega^{1/2}$. The Koutecky−Levich equation results in a plot of the inverse of the current density at a constant potential versus $\omega^{-1/2}$ that is linear with an intercept corresponding to i_k and a slope defined by c_0B, where $B = 0.62nFD^{2/3}\upsilon^{-1/6}$. The number of electrons transferred can be calculated by $n = (B/0.62F)D^{-2/3}\upsilon^{1/6}$.

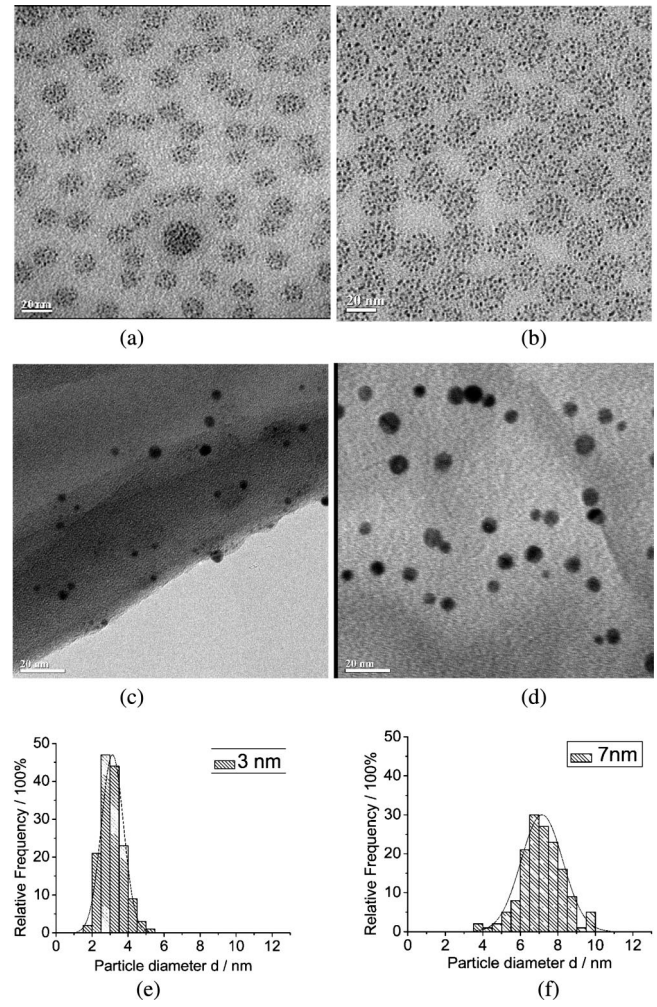

Figure 1. Transmission electron micrographs of micelle-encapsulated Au in solution: (a) 3 and (b) 7 nm. After calcination: (c) 3 and (d) 7 nm. Particle size distributions of calcined gold particles from TEM measurement: (e) 3 and (f) 7 nm.

2.5. Activation Energy Measurement. The activation energy measurement was based on the RDE measurements at three temperatures: 0, 23, and 50 °C. The samples were fitted onto the shaft of the RDE and immersed into the electrolyte, the three-neck electrode flask was placed in a constant-temperature bath, and the measurements performed as described above. The temperature-dependent solubility of oxygen in the electrolyte is taken into consideration when determining the activation energy. To account for the temperature-dependent oxygen concentration in the electrolyte in determining the kinetic current, the RDE measurements were performed for several oxygen partial pressures in the purge gas. The oxygen partial pressure was controlled by two mass flow controllers, for argon and oxygen, respectively. The total flow rate was 100 cm^3 min^{-1}. The volumetric flow ratios of argon and oxygen were 60:40,

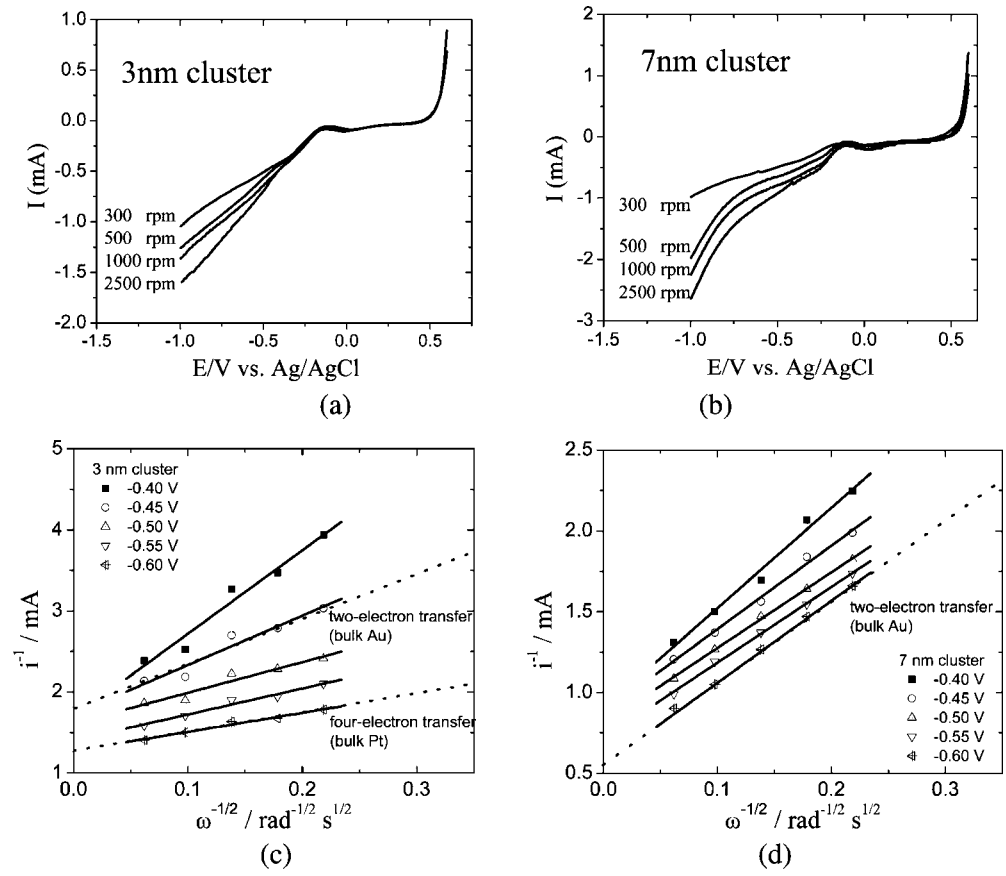

Figure 2. Oxygen electroreduction on 3 and 7 nm Au nanoclusters in oxygen-saturated 0.5 M KOH. Cyclic voltammograms (sweep rate 10 mV s^{-1}) of Au nanoparticles on carbon rotating disk electrodes at several rotation speeds: (a) 3 and (b) 7 nm clusters. Levich plots of the voltammogram data (the currents at −0.6 V were used): (c) 3 and (d) 7 nm clusters.

40:60, and 20:80. RDE measurements including a pure feed of oxygen and air were also performed.

3. Results and Discussion

3.1. Characterization of Size-Selected Au Nanoclusters. Prior to calcination, the sizes of the polymer-encapsulated Au particles formed using the PS(54300)−P2VP(8800) and PS-(53000)−P2VP(43800) polymers were observed by TEM to be 15 ± 2 nm (Figure 1a) and 30 ± 2 nm (Figure 1b), respectively. The metallic Au particle sizes were determined after ozone treatment to oxidize away the polymer coating (Figure 1c,d). The particle size distributions of the ozone-treated samples obtained from a sampling of 150 gold particles in several TEM images are shown in Figure 1e,f. The mean particle sizes were determined to be 3.1 ± 0.6 and 6.8 ± 1.1 nm, respectively.

3.2. Oxygen Reduction Reaction (ORR) on Size-Selected Au Nanoclusters Using the Rotating Disk Electrode (RDE). The linear sweep scans from samples of different size Au nanoclusters in oxygen-saturated solutions of 0.5 M KOH at several rotation speeds are shown in Figure 2a,b. The current density in the region from −1.0 to −0.6 V on the cathode corresponds to oxygen reduction on the Au nanoclusters, which is a function of the rotation speed in the diffusion-limited regime. The shape of each CV exhibits the capacitance of the carbon electrode. The active surface areas were determined by Cu-UPD.

From the cyclic voltammograms obtained with the RDE, Figure 2a,b, the currents at −0.6 V were used as a measure of oxygen reduction activity. The Levich plots generated from the data are shown in Figure 2c. The kinetic currents reflecting the mass transfer independent kinetics were calculated using the Koutecky−Levich equation and are listed in Table 1. The activity (kinetic current density, J_k) of the 3 nm gold clusters was ∼2.5 times greater than that of the 7 nm clusters. Although quantitative comparisons of the kinetic current densities between different systems requires caution, the values of 3.5 and 1.5 mA cm^{-2} obtained for the 3 and 7 nm clusters respectively at −0.6 V vs Ag /AgCl may be qualitatively compared to values published previously obtained from Pt/C at 7.8 mA cm^{-2} at −0.96 V vs Ag /AgCl in 1 mol·L^{-1} KOH solution,[14] Ag/C at 3.8 mA cm^{-2} at −0.96 V vs Ag /AgCl in O_2-saturated 1 mol·L^{-1} KOH solution,[14] and W_2C/C at 1.6 mA cm^{-2} at −1.11 V vs Ag /AgCl in 1 mol·L^{-1} KOH solution.[14] The reported kinetic current density from Co oxide doped Au ($Au_{98.77}Co_{1.23}O_x$) was 7 mA cm^{-2} at −0.4 V vs Ag/AgCl in 0.5 mol·L^{-1} KOH solution.[15] The 3 nm gold clusters have a lower kinetic current density than those reported previously, albeit obtained from significantly more negative potential regions.

TABLE 1: Levich Plot Parameters Determined from Data of Au Nanoparticles in Oxygen-Saturated KOH

	intercept (mA^{-1})	I_k (mA)	surface area (cm^2)	J_k (mA cm^{-2})	slope (mA cm^{-2})	n
3 nm (±1) clusters	1.21	0.83	0.24	3.5	2.5	4.1
7 nm (±1) clusters	0.56	1.79	1.22	1.5	4.7	2.1

From slopes in the Levich plots shown in Figure 2c,d, the numbers of electrons transferred in the process, n, were determined by the Koutecky−Levich equation using values for the same oxygen diffusion coefficient, D, of 1.9 × 10^{-5} cm^2/s,

the kinematic viscosity of the solution, v, of 9.97×10^{-5} cm^2/s, and concentration of oxygen in the bulk, c_0, of 2.5×10^{-6} mol/cm^3.

The Levich plots were extracted from cathodic scans between −0.40 and −0.60 V vs Ag/AgCl. For voltages more positive than −0.40 V, which is in the kinetic region, the measured currents had low signal-to-noise ratios and the kinetic currents and electron transfer numbers could not be reliably obtained. In control experiments with bulk gold and bulk platinum electrodes in the same electrolytes, the expected electron transfer numbers of 2 and 4 were obtained respectively in the same cathodic range (−0.40 to −0.60 V). For the larger 7 nm Au clusters a two-electron-transfer process was observed (as expected for bulk gold) at all applied potentials between −0.40 and −0.60 V (Figure 2d). The variability in the slopes obtained for the 3 and 7 nm clusters was within the experimental measurement error of ∼10%. In the Levich plots for the 3 nm Au clusters (Figure 2c), the slope was observed to decrease 4-fold as the bias was decreased from −0.40 to −0.60 V. This unusual behavior of the 3 nm nanoparticles indicates a bias-dependent change in the reduction pathway. At a potential of −0.40 V, the 3 nm nanoparticles exhibited an apparent electron transfer number less than 2, which was observed repeatedly on different samples of the same particle size. We speculate the possibility that a one-electron transfer corresponding to step 2a below occurs with an unexpectedly rapid desorption of the superoxide ion into the liquid phase with subsequent disproportionation.

$$2O_2^{\bullet -} + H_2O \rightarrow O_2 + O_2H^- + OH$$

At a more negative potential, −0.45 V vs Ag/AgCl, the Levich plot slope decreased to reflect an apparent two-electron transfer (step 3b). Finally, at electrode potentials between −0.50 and −0.60 V vs Ag/AgCl, the more efficient four-electron transfer was observed from the slope of the Levich plot. Further work will be needed to fully characterize this interesting observation and determine whether the apparent two-electron transfer was the simultaneous presence of a one-electron superoxide pathway with a four-electron process or a third, two-electron, pathway.

The values of n, 4.2 ± 0.5 and 2.1 ± 0.2 for 3 and 7 nm nanoparticles obtained from the Levich plots at −0.6 V, respectively, have an accuracy of approximately 10% limited by the roughness of electrode surface, where a planar electrode is assumed in the Koutecky−Levich equation. The two values can be assigned to four-electron and two-electron pathways for oxygen reduction in a basic electrolyte shown below. The four-electron reaction is more oxygen efficient for current production than the two-electron reaction.[16] The two pathways have a common intermediate of oxygen reduction, HO_2^-.[17–20] The four-electron pathway indicates the further reduction of HO_2^-. However, in the two-electron pathway, HO_2^- species may desorb into the solution and decompose into O_2 and OH^-. In the work of Kim et al.[21] on gold crystal surfaces in basic media, the two-electron pathway was investigated. In their study, they observed a superoxide intermediate by surface enhanced Raman scattering (SERS) but did not observe HO_2^- on the surface (see eq 3b),[21] because of desorption and decomposition to oxygen and hydroxide as shown in eqs 5b[13] and 6b,[21] respectively. The data from the 3 nm particles (Figure 2c) suggest a four-electron-transfer process and not the two-electron transfer observed by Kim et al.[21] on extended Au surfaces. We speculate that the high density of low coordination sites on the 3 nm nanoparticles may increase the activation of the peroxide intermediate, facilitating further reduction and the four-electron transfer. Having low coordination (edge and corner) with high electric field brings stronger OH^- adsorption to the surface, where the improvement of OH^- adsorption on polar surface was observed by Chen et al.[22] This possibly expedites the further reduction of HO_2^- adsorption to OH^- adsorption, as in eq 4a.

TABLE 2: Kinetic Currents for the 3 and 7 nm Au Nanoparticles in Oxygen-Saturated KOH at Three Temperatures

	7 nm			3 nm		
	50 °C	23 °C	0 °C	50 °C	23 °C	0 °C
I_k (mA)	1.39	1.25	0.79	0.43	0.38	0.34
I_k* [a] (mA)	2.14	1.25	0.47	0.53	0.38	0.26

[a] I_k* is the kinetic current corrected for the temperature-dependent oxygen concentration.

four-electron-pathway reaction

$$O_2 + * \rightarrow O_{2,ads} \quad (1a)$$

$$O_2 + e^- \rightarrow O_{2^-} \quad (2a)$$

$$O_2^-{}_{ads} + (H_2O + e^-) \rightarrow HO_2^-{}_{ads} + OH^-{}_{ads} \quad (3a)$$

$$HO_2^-{}_{ads} + (H_2O + 2e^-) \rightarrow 3OH^-{}_{ads} \quad (4a)$$

$$OH^-{}_{ads} \rightarrow OH^- + * \quad (5a)$$

two-electron-pathway reaction

$$O_2 + * \rightarrow O_{2,ads} \quad (1b)$$

$$O_{2,ads} + e^- \rightarrow O_2^-{}_{ads} \quad (2b)$$

$$O_2^-{}_{ads} + (H_2O + e^-) \rightarrow HO_2^-{}_{ads} + OH^-{}_{ads} \quad (3b)$$

$$OH^-{}_{ads} \rightarrow OH^- + * \quad (4b)$$

$$HO_2^-{}_{ads} \rightarrow HO_2^- + * \quad (5b)$$

$$2HO_2^- \rightarrow O_2 + 2OH^- \quad (6b)$$

3.3. Temperature Effects of Au Nanocluster Activity. To determine the effective activation energy for the ORR on the 3 and 7 nm nanoparticle catalysts, the kinetic rates were measured with the RDE at three different temperatures; see Table 2.

From the temperature-dependent linear sweep scans obtained on the RDE, the temperature-dependent kinetic currents which were found by fitting the Levich equation to the data are listed in Table 2. The temperature-dependent oxygen solubility, referenced from literature data,[23] was used to correct I_k to equivalent oxygen concentrations. By varying oxygen partial

TABLE 3: Kinetic Currents for the 3 and 7 nm Au Nanoparticles in Oxygen-Saturated KOH at Different Oxygen Partial Pressures

	7 nm				3 nm			
	1 bar	0.6 bar	0.4 bar	0.2 bar	1 bar	0.8 bar	0.6 bar	0.2 bar
intercept (mA^{-1})	0.80	2.48	3.34	5.18	2.67	2.15	2.79	4.63
I_k (mA)	1.25	0.4	0.3	0.19	0.38	0.47	0.36	0.21

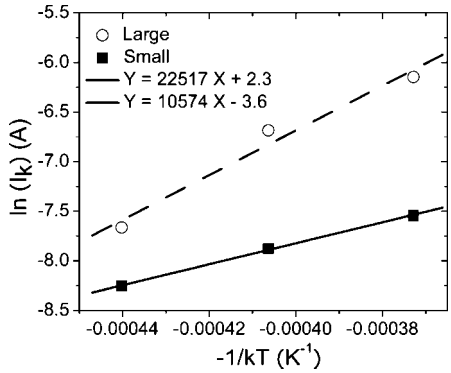

Figure 3. Oxygen electroreduction on 3 and 7 nm Au nanoclusters at variable temperatures. I_k was produced from the RDE experiment in oxygen-saturated 0.5 M KOH. The correlation of $\ln(I_k)$ and $-1/T$ results in the activation energy by the slope.

pressure in the feed gas, the I_k values were determined as a function of oxygen concentration; see Table 3. For the 7 nm clusters, the data are consistent with a first-order dependence of I_k on the oxygen concentration, whereas for the 3 nm clusters a half-order dependence is a better fit to the data. The change in the order of the oxygen dependence reflects the difference in the ORR mechanism between the two- and four-electron transfer. At three temperatures (0, 23, and 50 °C), the oxygen solubility is different; however, from the dependency, I_k can be corrected, I_k*, to the oxygen saturation concentration at room temperature (23 °C). The values of the currents corrected to room temperature are given in Table 2.

The corrected kinetic current densities at the three temperatures (0, 23, and 50 °C), Figure 3, were fit to an Arrhenius rate equation, and the effective activation energies were calculated to be 0.11 ± 0.01 and 0.23 ± 0.02 eV for the 3 and 7 nm clusters, respectively.

This activation energy largely reflects the likely relatively slow oxygen absorption step, $O_2 + * \rightarrow O_{2,ads}$.[17–19] A decrease in the particle size leads to an increase in the adsorbed oxygen coverage (θ_0). Lizuka et al.[24] found that, in the gas phase, oxygen molecules have much a higher adsorption on the surface of unsupported Au nanoparticles than on the Au bulk surface. One explanation is the presence of additional low coordination (edge and corner) atoms in smaller particles which are proposed to have higher oxygen binding of O_2 than on the terrace or on the smooth surface.[7,24] Another possible factor is the increase in Au(100) surfaces compared to Au(111) in the smaller gold particles which contributed to the four-electron pathway in the reduction of oxygen.[25] Adzic[6] and co-workers rationalized higher catalytic activity by the stronger O_2 adsorption on Au(100).

4. Conclusions

In this work it was demonstrated that Au nanoclusters synthesized by micelle encapsulation supported on carbon substrates typical of the material contemplated for industrial fuel cells are highly active for ORR in basic media. The activity of the nanoclusters for ORR varies inversely with the size of the cluster. The increased activity is at least partially explained by a 50% reduction in the apparent activation energy. We speculate that the decreased coordination of Au together with the decreased electrophilicity of the smaller clusters results in an increase in the O−Au bond energy with a corresponding decrease in the activation energy of the critical step of molecular oxygen dissociative chemisorption; thus, the rate-limiting step for oxygen reduction is facilitated.

Acknowledgment. This work was supported by the Mitsubishi Chemical Center for Advanced Materials (NRT-5) and the U.S. Department of Energy (DE-FG03-89ER14048). Facilities support was provided by the NSF−MRSEC funded Materials Research Laboratory (DMR05-20415). The authors thank Mr. Benjamin Schwarz for technical assistance.

References and Notes

(1) Antoine, O.; Bultel, Y.; Durand, R.; Ozil, P. *Electrochim. Acta* **1998**, *43*, 3681–3691.
(2) Genies, L.; Faure, R.; Durand, R. *Electrochim. Acta* **1998**, *44*, 1317–1327.
(3) Mayrhofer, K. J. J.; Blizanac, B. B.; Arenz, M.; Stamenkovic, V. R.; Ross, P. N.; Markovic, N. M. *J. Phys. Chem. B* **2005**, *109*, 14433–14440.
(4) Takasu, Y.; Ohashi, N.; Zhang, X. G.; Murakami, Y.; Minagawa, H.; Sato, S.; Yahikozawa, K. *Electrochim. Acta* **1996**, *41*, 2595–2600.
(5) Perez, J.; Gonzalez, E. R.; Ticianelli, E. A. *Electrochim. Acta* **1998**, *44*, 1329–1339.
(6) Adzic, R. R.; Markovic, N. M.; Vesovic, V. B. *J. Electroanal. Chem.* **1984**, *165*, 105–120.
(7) Haruta, M. *Catal. Today* **1997**, *36*, 153–166.
(8) Guerin, S.; Hayden, B. E.; Pletcher, D.; Rendall, M. E.; Suchsland, J. P. *J. Comb. Chem.* **2006**, *8*, 679–686.
(9) Chou, J.; Zhang, S. Y.; Sun, S. L.; McFarland, E. W. *Angew. Chem., Int. Ed.* **2005**, *44*, 4735–4739.
(10) Jaramillo, T. F.; Baeck, S. H.; Cuenya, B. R.; McFarland, E. W. *J. Am. Chem. Soc.* **2003**, *125*, 7148–7149.
(11) Chou, J.; Franklin, N. R.; Baeck, S. H.; Jaramillo, T. F.; McFarland, E. W. *Catal. Lett.* **2004**, *95*, 107–111.
(12) Ben Aoun, S.; Dursun, Z.; Sotomura, T.; Taniguchi, I. *Electrochem. Commun.* **2004**, *6*, 747–752.
(13) Roche, I.; Chainet, E.; Chatenet, M.; Vondrak, J. *J. Phys. Chem. C* **2007**, *111*, 1434–1443.
(14) Meng, H.; Shen, P. K. *Electrochem. Commun.* **2006**, *8*, 588–594.
(15) Lin, H.; Tang, W.; Kleiman-Shwarsctein, A.; McFarland, E. W. *J. Electrochem. Soc.* **2008**, *155*, B200−B206.
(16) Bard, A. J.; Faulkner, L. R. In *Electrochemical Methods Fundamentals and Applications*, 2nd ed.; Wiley: New York, 2000; p 335.
(17) Vassilev, P.; Koper, M. T. M. *J. Phys. Chem. C* **2007**, *111*, 2607–2613.
(18) Shao, M. H.; Adzic, R. R. *J. Phys. Chem. B* **2005**, *109*, 16563–16566.
(19) Blizanac, B. B.; Lucas, C. A.; Gallagher, M. E.; Arenz, M.; Ross, P. N.; Markovic, N. M. *J. Phys. Chem. B* **2004**, *108*, 625–634.
(20) Genies, L.; Bultel, Y.; Faure, R.; Durand, R. *Electrochim. Acta* **2003**, *48*, 3879–3890.
(21) Kim, J. W.; Gewirth, A. A. *J. Phys. Chem. B* **2006**, *110*, 2565–2571.
(22) Chen, A. C.; Lipkowski, J. *J. Phys. Chem. B* **1999**, *103*, 682–691.
(23) Perry, R. H.; Green, D. E. In *Perry's Chemical Engineering's Handbook*, 6th ed.; McGraw Hill: New York, 1984; pp 3−103..
(24) Iizuka, Y.; Tode, T.; Takao, T.; Yatsu, K.; Takeuchi, T.; Tsubota, S.; Haruta, M. *J. Catal.* **1999**, *187*, 50–58.
(25) Gao, F. F.; El-Deab, M. S.; Okajima, T.; Ohsaka, T. *J. Electrochem. Soc.* **2005**, *152*, A1226−A1232.

JP710929N